Research Article Vol. 32, No. 3 / 29 Jan 2024 / Optics Express 4564
Optics EXPRESS

Pre-ablation regime light-induced optical changes in nanometer thick metal films

ESTER ABRAM,[1,2,*] IGOR MILOV,[1,3] NIKOLAI ORLOV,[4] KLAASJAN VAN DRUTEN,[1,2] ERIK C. GARNETT,[4] AND PAUL PLANKEN[1,2]

[1]*Advanced Research Center for Nanolithography (ARCNL), Science Park 106, 1098 XG Amsterdam, The Netherlands*
[2]*Van der Waals-Zeeman Institute, Institute of Physics, University of Amsterdam, Science Park 904, 1098 XH Amsterdam, The Netherlands*
[3]*Center for Free-Electron Laser Science CFEL, Deutsches Elektronen-Synchrotron DESY, Notkestrasse 85, 22607 Hamburg, Germany*
[4]*Center for Nanophotonics, AMOLF, Science Park 104, Amsterdam, 1098 XG, The Netherlands*
[*]*e.abram@arcnl.nl*

Abstract: We report on small optical reflection increases after illumination of nanometer thick gold and aluminum thin films on different substrates with single, femtosecond 400 nm wavelength pump laser pulses, in a pre-ablation fluence regime. In this fluence regime, small, irreversible and subtle morphological changes of the sample are observed. Dark-field, scanning electron, and atomic force microscopy images reveal subwavelength spallation features in the aluminum, and delamination in the gold layers in this pre-ablation regime. All of these morphological changes coincide with minute optical increases in the reflectivity, at the 0.1 – 2% level, as observed in-situ with a weak probe beam. From Liu-analysis, transfer-matrix, and two-temperature model calculations, we infer that in this pre-ablation regime, the aluminum layers already reach the melting temperature. Electron Backscatter Diffraction measurements show that the Al grains melt and resolidify into bigger grains. This suggests that for Al, resolidification into bigger grains is responsible for both the increased reflection, and the spallation in the pre-ablation regime. For gold, the optical change is most likely due to the etalon effect caused by delamination.

1. Introduction

In the semiconductor manufacturing industry, increasingly high optical powers, used in metrology, heighten the risk of optical damage.

While much light-induced damage research has been done on bulk gold [1,2] and/or aluminum [3–6], or on layers that are micrometers thick and thus qualify as bulk materials for fluences close to the damage threshold, semiconductor devices typically consist of thin films with thicknesses ranging from several, to hundreds of nanometers. For metrology applications it is clear that ablation [1,7–13], the rapid removal of material upon optical excitation, or other large film deformations [14,15], should be avoided at all times. In this high fluence regime, one has looked extensively into transient effects upon laser excitation [5,16–19].

Interestingly, subtle changes can already be induced by light fluences below the ablation threshold. From an applications perspective, it is essential to investigate this pre-ablation fluence regime on thin films to understand the underlying mechanisms and to study whether in situ optical probe techniques can be used to detect these changes before catastrophic damage occurs.

In this study, we look at the aftermath of pump-induced reflection and transmission changes in tens of nanometers thick gold and aluminum layers in a fluence regime below that of where catastrophic damage occurs. When probing the exposed regions more than one millisecond after exposure, when all transient effects have disappeared, we observe optical reflection and

#507689 https://doi.org/10.1364/OE.507689
Journal © 2024 Received 19 Oct 2023; revised 12 Dec 2023; accepted 27 Dec 2023; published 26 Jan 2024

Optics EXPRESS

transmission changes as small as 0.1% in a fluence regime before the onset of crater formation (ablation). For thin gold layers, scanning electron microscopy (SEM) and atomic force microscopy (AFM) strongly suggest that this increase is caused by delamination. This creates a void between the metal and substrate that leads to constructive interference in the reflecting direction. This observation is supported by transfer-matrix calculations [20,21]. For aluminum, we do not observe delamination. Instead, Electron Backscatter Diffraction (EBSD) measurements suggest that we can attribute the positive reflection change to melting and resolidification into larger grains of the aluminum. In addition, optical dark-field microscopy shows an area with bright spots that grows in size for increasing fluences. SEM and AFM images reveal that each spot in the area corresponds to groups of grains that are either slightly elevated with respect to the surrounding surface, or missing entirely. Liu-analysis [22], as well as two-temperature model (TTM) calculations [23–25], suggest that this spallation is a thermally driven process.

Our results provide new insights into the pre-ablation fluence regime: the fluence regime where light begins to affect materials before catastrophic damage occurs. As these morphological changes coincide with subtle changes in the optical reflectivity, the optical change can act as an early warning signal to prevent further damage.

2. Experimental details

2.1. Sample fabrication

8 to 80 nm thick gold and 10 to 30 nm aluminum layers are deposited by electron-beam physical vapor deposition (Polyteknik Flextura M508 E) on 0.5 mm borosilicate glass substrates, which have been cleaned in a base Piranha solution. Borosilicate glass [26] is chosen because of the negligible absorption of the 400 and 800 nm light. For comparison, in order to characterize substrate dependence, also sapphire, CaF_2 and silicon substrates were used. An overview of the samples used in the experiments is listed in Supplement 1. Additionally, relevant gold and aluminum properties are given in table 1.

Table 1. Optical and thermal mechanical properties of gold and aluminum.

	Au	Al
$n + ik$ @ 400 nm	$1.4684 + 1.9530i$[a]	$0.31448 + 3.8005i$[b]
$n + ik$ @ 400 nm ellipsometry	$1.57 + 1.89i$	$0.68 + 4.34i$
$n + ik$ @ 800 nm	$0.15352 + 4.9077i$[a]	$1.8385 + 6.9757i$[b]
$n + ik$ @ 800 nm ellipsometry	$0.23 + 4.74i$	$2.25 + 7.30i$
T_m (K)	1337.33[b]	933.47[b]
Native oxide thickness (nm)	None	4 nm
k_0 ($Wm^{-1}K^{-1}$)	318[d]	246[e]
C_i (10^6 $Jm^{-3}K^{-1}$)	2.4[f]	2.42[e]

[a]Ref. [27],
[b]Ref. [28],
[c]Ref. [29, p.6-146 and p.6-148].
[d]Ref. [30].
[e]Ref. [31].
[f]Ref. [32].

2.2. Set-up

The pump-probe set-up used for the experiments is shown schematically in figure 1. A multi-pass Ti:Sapphire amplifier generates 45 fs laser pulses with a central wavelength of 800 nm at a repetition rate of 1 kHz. The output of the laser is split by a 99/1 beamsplitter into a strong pump

Optics EXPRESS

and a weak probe beam. The pump is frequency-doubled in a Beta Barium Borate (BBO) crystal to a wavelength of 400 nm. It then passes through a 10% duty-cycle chopper which lowers the repetition rate to 100 Hz. This repetition rate is low enough for a galvo mirror to pulse-pick single pulses. The pump is reflected on three consecutive dichroic mirrors to filter out the fundamental beam. Both the pump and probe beam are focused onto a sample to a spot size of 70 μm and 15 μm FWHM respectively so that the pump spot is probed where the fluence varies only a little bit. The angle α, the angle of the probe beam with the normal of the sample, is approximately 10°. The pump illuminates the sample at near-normal incidence. In our pump-fluence-dependent single-shot measurements, the sample is moved automatically by the XY-translation stage. In this way, every new pump shot hits a pristine site. Between subsequent shots, a piezoelectric rotation mount rotates a $\lambda/2$ plate, placed before the BBO crystal, to change the pump pulse fluence.

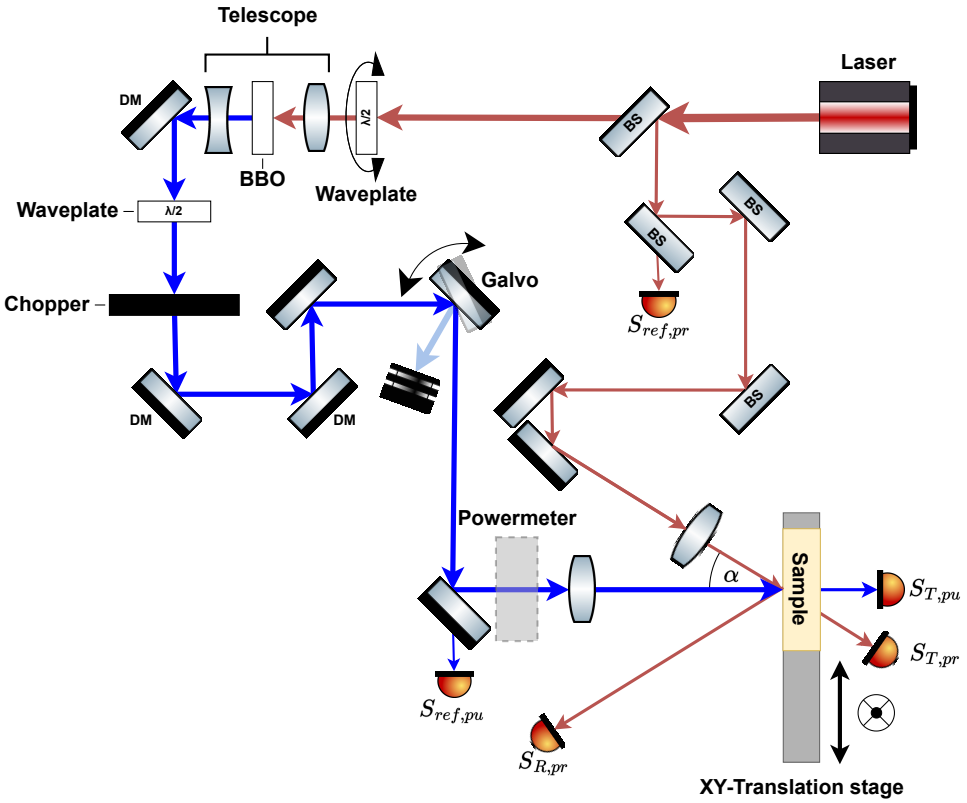

Fig. 1. Schematic of the experimental set-up. The 45 fs, 800 nm laser output is split into a strong pump and a weak probe beam. The pump beam passes through a telescope and a Beta Barium Borate (BBO) crystal to frequency-double it to a 400 nm wavelength. The pump beam is reflected by three consecutive dichroic mirrors (DM) to filter out the fundamental beam. Next, it passes through a $\lambda/2$-plate after which the beam is p-polarized, a chopper to lower the repetition rate to 100 Hz, and a galvo mirror to pulse-pick a single pulse. The pump beam is focused using a f = 20 cm lens and the sample is placed a short distance before the focal point. The pump is at normal incidence on the sample and the probe beam is at an angle α of $\approx 10°$ with respect to the normal. The power of the probe beam is attenuated by reflecting the beam off three beamsplitters (BS) before it is focused onto the sample. The pump pulse energy can be varied by rotating the first $\lambda/2$-plate. The location of the powermeter used during calibration is indicated.

Optics EXPRESS

In total, five switchable-gain Si detectors are used (Thorlabs PDA100A2) in the experiment, all of which are shown in figure 1. Two of these measure the pump and probe reference signals ($S_{ref,pu}$ and $S_{ref,pr}$), one the probe reflection signal ($S_{R,pr}$) coming from the sample, and two the pump and probe transmission signals ($S_{T,pu}$ and $S_{T,pr}$). The pump reference signal is the pump light leaking through the mirror placed in front of the focusing lens. The probe reference signal is formed by light transmitted by the 2/3 beamsplitter. All detector signals are digitized by an analogue-to-digital converter (ADC) and collected by a computer. The signals $S_{R,pr}$ and $S_{ref,pr}$ are first send to a boxcar averager (SRS SR250 2ns Gated Integrator) before being digitized. This is done for each individual shot produced by the laser. In addition, the chopper and galvo state (blocked or open) and the sample position are recorded. Before each measurement series, a Gentec-EO Beamage-4M beamprofiler is placed at the sample position to obtain the pump and probe beam profiles. Furthermore, a Coherent thermopile powersensor is placed in the pump beam path after the last mirror before the focusing lens. This is to calibrate the reference photodetector in order to convert the detector signal into a pump fluence (see Supplement 1).

2.3. Measurements/experimental procedure

Figure 2 is a schematic depiction of the experiment. Before each pump shot, 999 probe pulses illuminate a pristine spot on the sample. This is followed by one pump and one additional probe shot after which a thousand more probe shots hit the spot, potentially damaged by the pump. After this, the sample is translated and the measurement is repeated for a different pump fluence F. The reflectivity of, and the transmission through the sample of each probe shot are measured by the photodetectors and used to calculate the pump-induced changes in the reflection as follows:

$$\bar{R}_{pre} = \frac{\sum_{n=1}^{999} \frac{S_{R,pr,n}}{S_{ref,pr,n}}}{999}, \tag{1a}$$

$$\bar{R}_{post} = \frac{\sum_{n=1001}^{2000} \frac{S_{R,pr,n}}{S_{ref,pr,n}}}{1000}, \tag{1b}$$

$$\Delta R = \frac{\bar{R}_{post} - \bar{R}_{pre}}{\bar{R}_{post}}, \tag{1c}$$

where n is the probe pulse index and $S_{R,pr,n}$ and $S_{ref,pr,n}$ are the measured reflection and reference signals of the probe (see figure 1). Therefore, $\bar{R}_{pre}$ is the average relative reflectivity before, and $\bar{R}_{post}$ after pump illumination. ΔR is defined as the pump-induced *relative reflection change* of the probe. The pump-induced *relative transmission change* of the probe (ΔT) is obtained in a similar fashion.

In a typical experimental cycle, the pump pulses hit the sample in a six-by-six grid where each subsequent pump shot has a slightly higher fluence. To check reproducibility, each such cycle is repeated several times, leading to the formation of multiple grids.

2.4. Post-processing

After each measurement series, the sample is taken out of the laser set-up for inspection of the illuminated sites. First, each grid containing 36 illuminated sites, is inspected by Differential Interference Contrast (DIC/Nomarksi) and dark-field (DF) microscopy. Subsequently, a Helios Nanolab 600 scanning electron microscope (SEM) is used to study possible changes in morphology. Selected sites are inspected further with a Bruker Dimension Icon atomic force microscope (AFM). For some sites, Electron Backscatter Diffraction (EBSD) is used to map the crystal orientation and structure and to obtain grain sizes. EBSD was performed using an EDAX Clarity direct detector. The patterns were collected using EDAX APEX software, 100 pA beam current, 8 kV accelerating voltage and 200 ms pixel integration. The patterns were postprocessed using

Optics EXPRESS

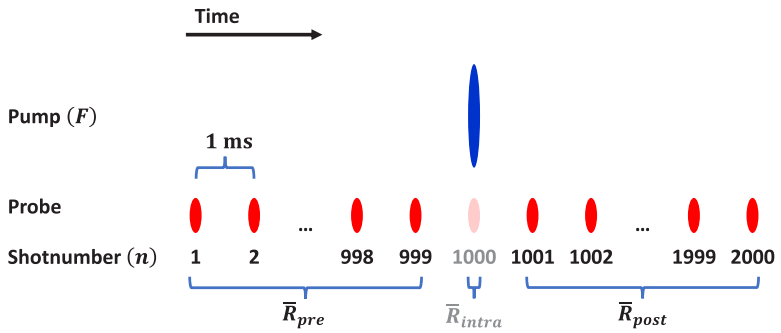

Fig. 2. Schematic overview of the pulse train that is incident on each individual site on a sample. The first 999 probe shots form the pre-pump reflectivity $\bar{R}_{pre}$ and shot 1001 to 2000 the post-pump reflectivity $\bar{R}_{post}$ (see Eq. (1)). The first probe pulse that samples the post-pump reflectivity arrives 1 ms after the pump pulse, when all pump-induced transient effects have disappeared. Note that probe pulse 1000 ($\bar{R}_{intra}$), which coincides with the pump pulse, is omitted in the analysis.

EDAX OIM software. All obtained patterns were indexed using Spherical Indexing with the Al phase (Fm-3m space group) and did not fit to the γ-Al_2O_3 phase (Fd-3m space group). This is in full agreement with literature data [33,34], which reports that the Al_2O_3 film grows in amorphous form. Therefore, the aluminum oxide does not generate any EBSD signal.

If the assumption that the fluence at the observed crater edge is equal to the threshold fluence F_{abl} is correct, a simple analysis can be used to extract that fluence from the data using a so-called Liu-analysis [22]. This analysis is valid for (elliptical) Gaussian beams with a peak fluence F_0. The crater area A and the natural logarithm of the fluence, $\ln(F_0)$, then follow a linear relation. When plotting A versus $\ln(F_0)$ in a so-called Liu-plot, the values a and b of the linear regression line $A = a\ln(F_0) + b$ are obtained. This is used to obtain the desired ablation threshold fluence F_{abl} and the FWHM of the gaussian beam waist d_x (long axis) and d_y (short axis),

$$F_{abl} = \exp(-\frac{b}{a}), \tag{2a}$$

$$d_x = \sqrt{\frac{4\ln(2)a}{\pi c}}, \tag{2b}$$

$$d_y = d_x c, \tag{2c}$$

The ratio $c = \frac{d_y}{d_x}$ can either be directly obtained from the crater dimensions or taken from the measured beam profile. A more detailed derivation of Eqs. (2a–2c) can be found in Supplement 1. Note that all values F given in this paper are defined as the pulse energy divided by the area bounded by the FWHM of the (elliptical) gaussian beamprofile. This effective fluence F is equal to the peak fluence F_0 divided by ln(2) (see Supplement 1). Both the effective fluence F and effective diameter d used throughout this paper equal:

$$F = \frac{F_0}{\ln(2)}, \tag{3a}$$

$$d = \sqrt{d_x d_y}. \tag{3b}$$

3. Results and discussion

Single layers of gold with thicknesses between 8 to 80 nm and aluminum with thicknesses from 10 to 30 nm on 0.5 mm borosilicate glass were illuminated with a strong pump pulse while being

Optics EXPRESS

probed by a weak probe beam as described in subsection 2.3. A permanent change in the material occurs for illuminated sites for which the pump-induced relative reflection (ΔR, see Eq. (1)) and transmission changes (ΔT) are nonzero. By comparing these values with Nomarski, dark-field, scanning electron (SEM) and atomic force microscopy (AFM) images of these sites, an in depth, thickness-dependent analysis of the damage mechanisms for thin gold and aluminum layers is obtained. As an example, Figure 3 shows the Normarski (a), dark-field (b), SEM (c, f) and the height (d) and phase (e) AFM profile images of the same six-by-six grid. This grid is formed by 36 single pump pulses of increasing fluence on a 20 nm thick Au layer. For fluences higher than the ablation threshold (F_{abl}), the crater edge is clearly visible as the dark ellipses in the Nomarski microscopy images. Because of the steepness of the ablation edges, these edges appear with a very high contrast in the dark-field images. Therefore, the dark-field images are well suited to obtain crater sizes. These sizes are obtained by using Canny edge detection [35] and the Halir and Flusser ellipse detection algorithm [36] on the dark-field images. Subsequently, the crater sizes are used to obtain the thresholds (F_{abl}) and spot sizes by Liu-analysis [22].

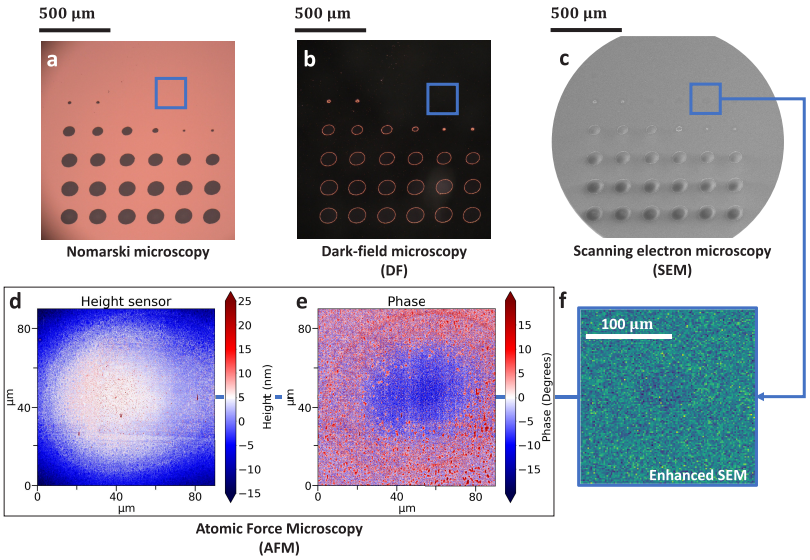

Fig. 3. Nomarski (a), dark-field (b), and SEM (c) images of the same illuminated six-by-six grid on a 20 nm Au layer on borosilicate glass. The AFM scan (d and e) and numerically enhanced SEM (f) are taken of the same pre-ablation site (regime II, $\Delta R>0$) marked with the blue square in a-c. Since tapping-mode is selected both the height (d) as well as the phase (e) profile is obtained.

For aluminum, a few sites are inspected by Electron Backscatter Diffraction (EBSD). This is used to map the crystal orientation and to study grain sizes, the results of which are presented in section 3.4.

3.1. Gold

Although gold is not commonly used in the semiconductor manufacturing industry, its optical and thermal mechanical properties are well-studied and known [2,37–40]. In addition, it does not react with the ambient atmosphere, making it a logical choice as a material for the first experiments. Figure 4 shows the change in the probe reflectivity (Eq. (1)) as a function of pump fluence for 20 nm of Au on a 0.5 mm thick borosilicate glass substrate.

Figure 4 shows that $\Delta R(F)$ can be divided into three fluence regimes:

Optics EXPRESS

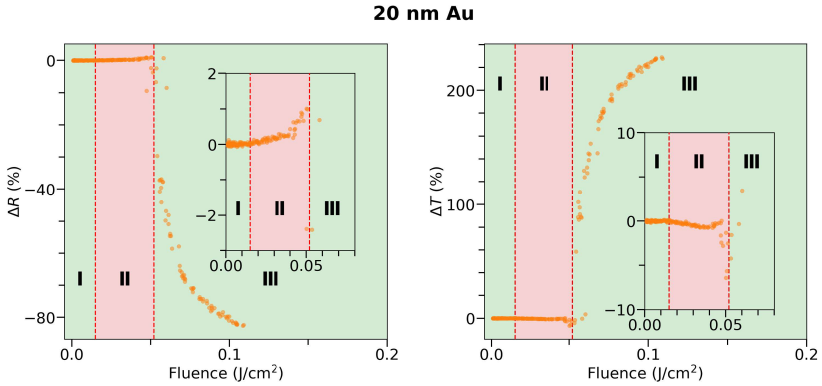

Fig. 4. Relative probe reflection ΔR (left) and transmission ΔT (right) change versus pump fluence F for 20 nm gold on a 0.5 mm borosilicate glass substrate. I, II and III mark the low ($\Delta R = 0$), medium ($\Delta R>0$) and high fluence ($\Delta R<0$) regimes respectively. The red lines mark corresponding thresholds between those regions.

I. **Low fluence regime**: Here the reflectivity is not affected by the pump ($\Delta R \approx 0$)

II. **Medium fluence regime**: There is a slight (positive) ΔR of a few percent only, induced by the pump ($\Delta R>0$)

III. **High fluence regime**: ΔR becomes negative due to a steep ΔR decrease ($\Delta R<0$ and $\partial \Delta R/\partial F<<0$)

Note that the same holds for ΔT but with opposite sign and therefore, in what follows, we will focus on ΔR only.

In regime I, the pump fluence is too low to permanently affect the illuminated site. Inspection of those sites with AFM and SEM showed no morphological or any other light-induced changes, as schematically indicated in Fig. 5(a). For high fluences (regime III), ablation is seen in the form of removal of material from the substrate, leaving a crater. Because of this, the reflectivity of the probe will drop and the transmission will increase with respect to the initial state. The bigger the crater, the lower the reflectivity, as schematically shown in Fig. 5(c) and (d). However, the way the pump influences the illuminated sites in regime II is less straightforward. SEM images show an elliptical region with a slightly darker shade at the regime II-illuminated sites. However, this shading is only visible when numerically enhancing the contrast of a grid image as is shown in Fig. 3(f).

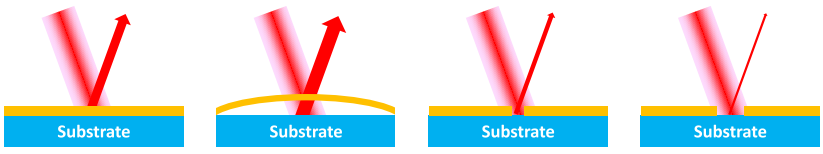

(a) $\Delta R = 0$ (b) $\Delta R > 0$ (c) $\Delta R < 0$ (d) $\Delta R < 0$

Fig. 5. Four examples of possible pump-induced changes in the thin Au film. The thickness of the arrow indicates the strength of the probe reflectivity. $\Delta R = 0$ for low pump fluences (a), while for intermediate fluences, $\Delta R>0$ (regime II), which can be caused by void formation due to delamination (b). For high fluences, the ablation regime is reached (regime III). For increasing crater sizes, the reflectivity will decrease until the entire probe spot fits inside the crater (c-d).

Optics EXPRESS

To study the effect of the thickness of the gold layer, six samples with different thicknesses were fabricated in one run. Each time when (a multiple of) 8 nm was deposited, a shutter repositioned by which a new part of the substrate array was exposed. Therefore, all six samples were made under comparable vacuum conditions, evaporation pressures and deposition rates. Figure 6(a) shows the relative probe reflection change ΔR versus the pump fluence for these six samples with thicknesses ranging from 8 to 80 nm. The insets show the individual data with a zoomed-in vertical axis. The vertical dashed lines are the inferred ablation thresholds F_{abl} and the gray areas mark the corresponding uncertainty obtained from the Liu-analysis. The layers with thicknesses from 16 to 40 nm display a positive ΔR increase for fluences lower than the ablation threshold. For the 8 nm thickness there is a negative ΔR. However, this thickness is close to the percolation threshold and the layer is therefore not continuous. The 80 nm thick film does not display a ΔR change in the pre-ablation regime. Figure 6(b) is the corresponding Liu-plot in which the lines are the obtained Liu-fits (see section 2.4). From these linear regression lines, the ablation threshold fluence F_{abl} and the FWHM of the beam profile d are obtained and are given in Table 2.

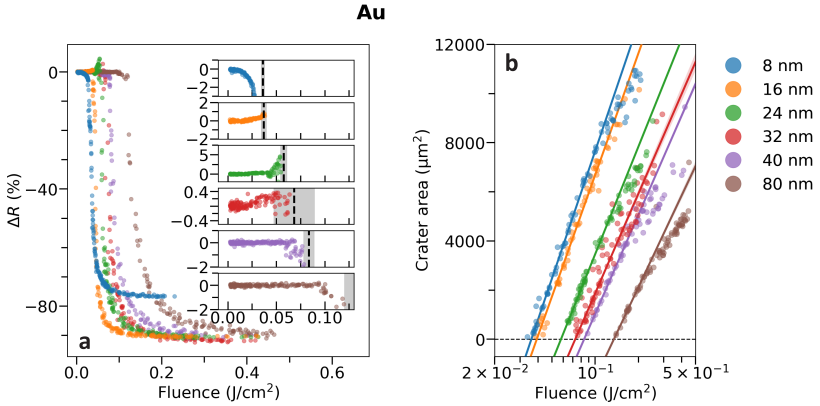

Fig. 6. (a) ΔR versus fluence F for gold layers on borosilicate glass with thicknesses of 8, 16, 24, 36, 40 and 80 nm respectively. The insets show the individual data zoomed in on the vertical axis. The vertical dashed lines are the ablation thresholds and the gray area the corresponding error obtained by Liu-analysis. (b) is the Liu-plot of these gold films. In the Liu-plot, the crater area is plotted versus the natural logarithm of the pump fluence. The lines are the corresponding linear fits for each sample. The intersection of those lines with the horizontal axis is the ablation fluence F_{abl} and the slope gives the pump spot size (see subsection 2.3). The slope is slightly different for the different layers which indicates that the spot size on the sample is different. This is mainly due to repositioning of new samples into the set-up giving rise to small variations in sample distance with respect to the focal point.

Table 2. Ablation threshold fluences and inferred laser illumination diameters, including fitting uncertainties for gold, obtained by Liu-analysis.

Thickness (nm)	F_{abl} (mJ/cm^2)	d (μm)
8	36 ± 0.28	81.3 ± 0.3
16	39 ± 1.0	79.4 ± 0.6
24	56 ± 1.0	74.7 ± 0.4
32	73 ± 4	72 ± 1.3
40	84 ± 2.4	71.7 ± 0.6
80	135 ± 8	69 ± 1.1

Optics EXPRESS

In fluence regime II, before the ablation thresholds, all Au sample thicknesses, except for 8 and 80 nm, display a (small) positive ΔR, and at the ablation threshold, there is a steep ΔR decrease. As already mentioned, SEM images of regime II-illuminated sites appear to be slightly darker than unilluminated sites, but the contrast is low, see Fig. 3(c). Comparing the grain structure with that of a pristine site shows no discernible difference. However, a large-area AFM scan such as shown in Fig. 3(d), indicates that the gold layer is slightly elevated in the center. The adhesion of gold to glass is known to be weak and SEM images of ablated sites (example shown in Fig. 7) clearly illustrate that delamination has occurred at high fluences. One hypothesis for the small positive ΔR in fluence regime II is that before the film ruptures, which occurs at high fluences in regime III, a void is formed between the Au layer and the glass as schematically depicted in Fig. 5(b). The phase profile of the AFM scan in Fig. 3(e) shows a faint elliptical outline (reddish curve in Fig. 3(e)). The phase signal is not only sensitive to the height changes and adhesion strength between the tip and the layer, it is also sensitive to the viscoelasticity of the layer. Therefore, the faint elliptical outline might indicate a local change in (bending) stiffness of the layer, and thus can be an indication of the edge of the buried void. However, it is challenging to draw direct conclusions from discrepancies in AFM phase images, as subtle as shown here. Nevertheless, the local fluence at the outline of the ellipse is calculated using the dimensions from the AFM scan and known spot size. This local fluence is ≈ 16 mJ/cm^2 which equals the threshold value between the $\Delta R = 0$, and $\Delta R>0$ regime as shown in (the inset of) Fig. 4. Therefore, the area within the ellipse corresponds both to an increase in height, and it marks the $\Delta R>0$ area.

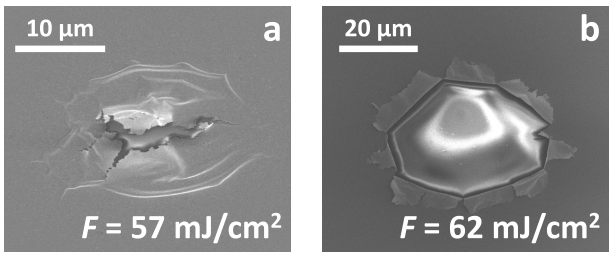

Fig. 7. SEM images of two ablation sites of a 20 nm gold layer on 0.5 mm borosilicate glass for two different fluences. For a fluence just above the ablation threshold (a), folds start to appear around the ripped center. At a higher fluence (b) flaps have formed at the crater sides while there is no indication of melting.

The combination of the gold layer, void and the substrate forms an etalon for the probe beam, which changes the reflectivity of the stack. Because the penetration dept of gold is ≈ 16 nm at a wavelength of 800 nm [27], this etalon effect will not be seen by the probe in thicker layers. This would also explain why there is no significant ΔR increase for the 80 nm thick layer. If the ΔR increase is not due to the etalon effect but to a (morphological) change throughout the entire layer or at the void-gold interface, this effect would also be apparent at the 80 nm thick layer. The 8 nm thick layer has a thickness around the percolation threshold of gold [41], making this layer structurally and optically significantly different from the others.

3.2. Aluminum

Unlike gold, aluminum is commonly used in the semiconductor manufacturing industry [42]. Because of its strong adhesion to glass and the presence of an oxide layer that forms rapidly, aluminum layers are expected to behave differently from gold layers. Figure 8(a) shows the measured pump-induced relative reflection change ΔR versus the pump fluence F for a 20 nm thick aluminum layer on 0.5 mm borosilicate glass. The datapoints marked in green, red and

Optics EXPRESS

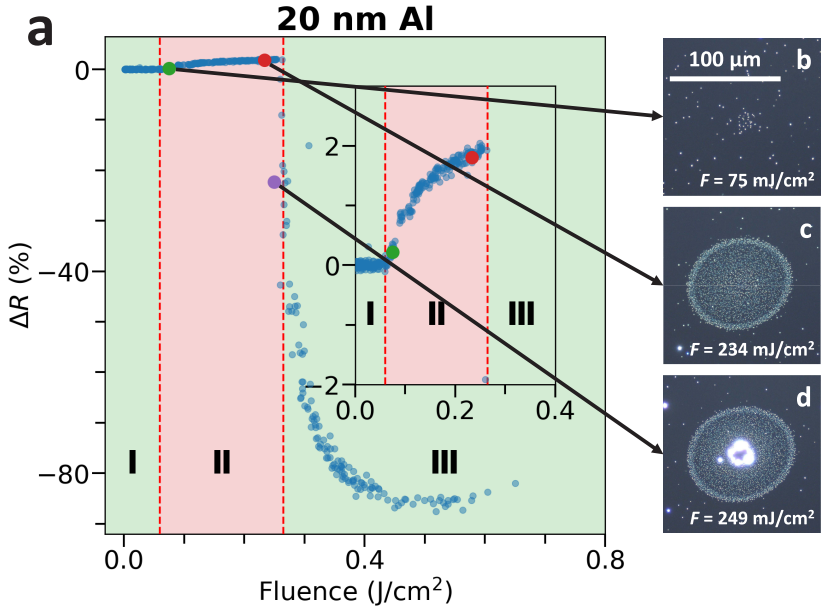

Fig. 8. Relative reflection change ΔR versus fluence F of 20 nm aluminum on borosilicate glass. I, II and III mark the low ($\Delta R = 0$), medium ($\Delta R>0$) and high fluence ($\Delta R<0$) regimes respectively. The red dashed lines mark corresponding boundaries between those regions. The inset shows a zoom-in to the regime II of the main graph. The dark-field microscopy pictures correspond to the following three datapoints: Just beyond the spallation threshold (green, b), just below ablation (red, c) and just beyond the ablation threshold (purple, d).

purple correspond to the optical dark-field images in Figs. 8(b-d). At a pump fluence where ΔR begins to increase slightly (green datapoint, regime II), Fig. 8(b) shows that bright spots, locations of increased scattering, start to appear in a location that corresponds to the center of the pump pulse. For increasing fluences, the area covered with these spots increases and a ring with a somewhat higher density of spots develops as shown by Fig. 8(c). Figure 8(d) shows that the spots are also visible in the ablation regime, outside of the ablated area, were the ablation area is defined by the small, brighter ring in the center. In Supplement 1, a dark-field image containing a single six-by-six grid is presented containing 36 illuminated areas at different pump fluences, as well as a dark-field image of a pristine site. This image can be used to gain a better insight into the spallation-onset fluence and the pristine material conditions.

In Fig. 9(a-c), we show a dark-field, SEM and an AFM image of the same area presented in Fig. 8(b) where bright spots are formed. As can be seen, the bright spots appear as dark spots in the SEM images. The corresponding AFM image shows a height difference at those spots. By further zooming in on these groups of grains, as shown by the SEM image in Fig. 9(d), it appears that these spots have an irregular shape and appear to follow grain boundaries. Since the oxide is expected to be amorphous [34], these grain boundary lines might originate from the pristine aluminum layer the oxide grew on. The shape of the spots marked by A and B in Fig. 9(d) correspond to a slight depression and elevation respectively in the AFM height map shown in Fig. 9(e). This AFM image shows that spot A corresponds to an area that is $\approx$ 4 nm lower than the area surrounding the spot. This suggests that a group of grains has been removed from the layer. At spot B, a group of grains seems to have been partially pushed upwards, sticking out of the pristine surface. Both A and B type spots are present in the 14 to 30 nm thick aluminum layers that have been studied. However, for layers of 22 nm and more, the groups of missing

Optics EXPRESS

grains dominate. For layers having a thickness of 20 nm and lower, the group of grains that are sticking out from the surface dominate. An example of this is shown in Fig. 10(a and c) where we plot the height profiles obtained by tapping mode AFM. Figure 10(a) shows two grains that stick out of the surface of an 18 nm thick aluminum layer, whereas Fig. 10(c) shows multiple grains that are missing from a 22 nm thick aluminum layer. Figure 10(b and d) are the corresponding phase images. These phase maps display a significant negative phase jump at the spallated sites. This means that, at the spallated sites, the AFM tip bounces back with a slight delay indicating that the viscoelasticity of the layer is different or interaction of the forces between the tip and the layer has changed [43]. Nevertheless, the contrast of this phase jump where groups of grains are sticking out from the surface is lower than where they are missing. This can be caused by the fact that at the missing grains site, the native oxide layer has been removed and a new slightly different oxide layer is formed on the affected aluminum. At positions where the groups of grains are elevated, the original native oxide is still present.

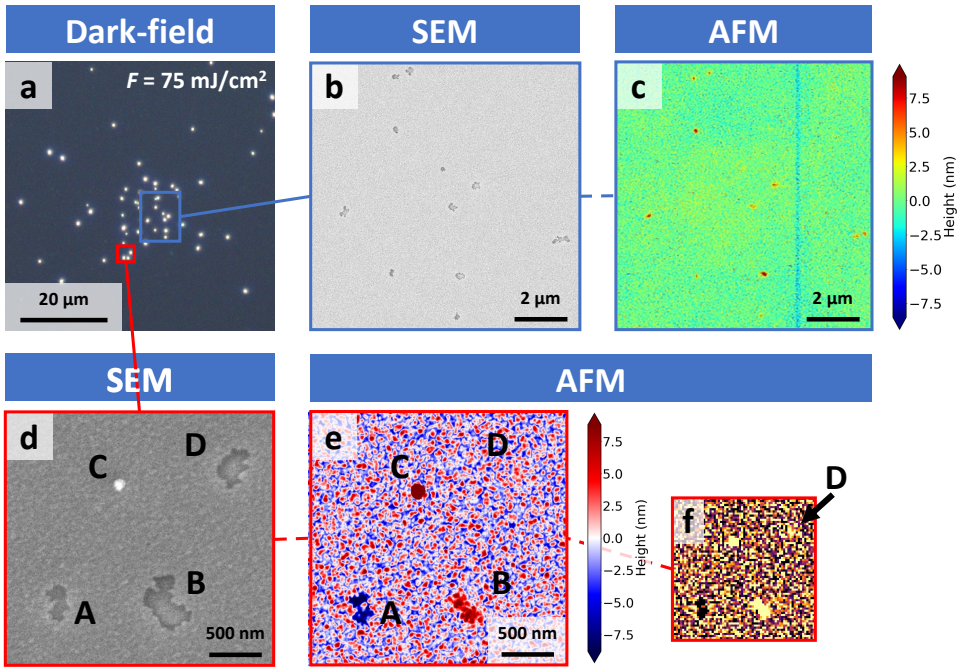

Fig. 9. Optical dark-field image (a) of a regime II ($\Delta R>0$) illuminated spallated site of a 20 nm aluminum layer on borosilicate glass. (b) SEM and (c) AFM image of the area marked by the blue rectangle in the dark-field image. (d) and (e) SEM and AFM scans of the area marked by the red rectangle in figure (a). Lowering the resolution and enhancing the contrast of figure (e) resulted in figure (f). The group of grains marked by A and B look similar in the SEM image. However the AFM scan shows that the group of grains marked by A is missing from the surface, while the grains marked by B are sticking out of the surface. Note that the contrast of SEM image (b) is enhanced for the purpose of this paper. The original picture is darker, indicating decent conduction. Note that D also marks a pushed up group of grains. However, it is somewhat difficult to see this by eye from the AFM scan in figure (e), but it shows up more clearly in (f) where the same data is shown but with enhanced contrast and lower resolution. Because the area marked by C is not present in the dark field picture (a), it is probably a dust particle that has settled on the surface after acquiring dark-field pictures and before performing the SEM and AFM scan.

Optics EXPRESS

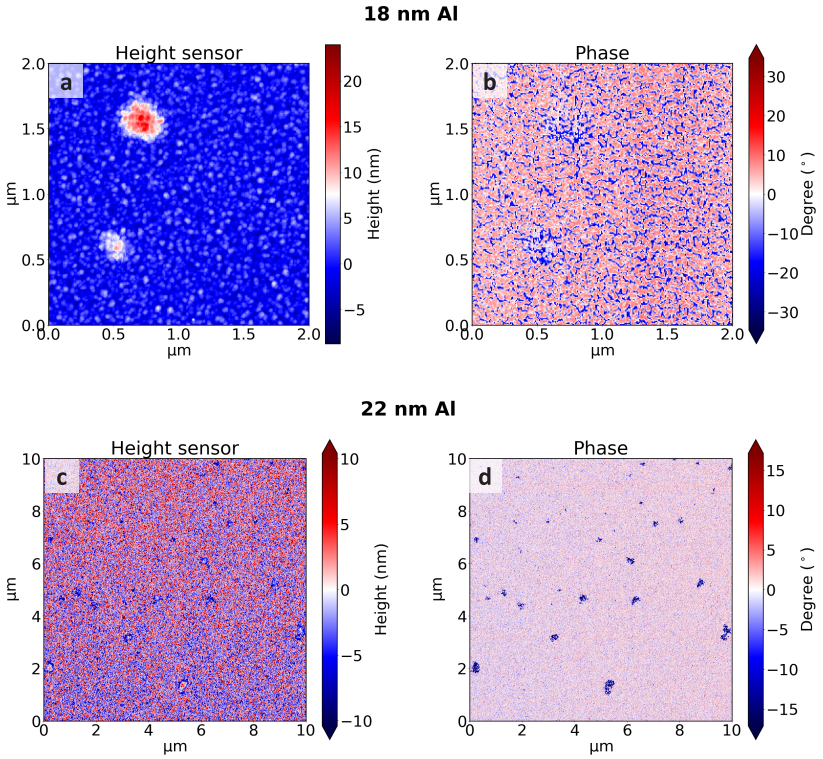

Fig. 10. AFM tapping mode height and phase profiles after illumination with a 400 nm pump pulse in the pre-ablation fluence regime. A detail of the height (a) and phase (b) profiles of a 18 nm thick aluminum layer on glass. (c) and (d) are the height and phase profile of a detail of an AFM scan of a 22 nm thick layer of aluminum. For the 18 nm thick layer, (a) shows two groups of grains sticking out of the surface. They are both weakly visible in the phase image (b). For the 22 nm thick layer, (c) displays multiple groups of missing grains which are clearly visible in the phase image (d). The missing grains, as well as the groups of grains that are sticking out of the surface, are also visible in the phase image by a slight phase drop.

Each spot in a dark-field image resembles a group of missing grains, or a group of grains sticking out of the surface. We hypothesize that the group of grains sticking out of the surface is representative of an intermediate stage, before the complete removal of the grains. From here on, we will refer to both processes as *spallation*.

Figures 11(a and b) show a dark-field image and a zoomed-in version of a site illuminated by a high-end regime II-fluence. For these fluences, the spallation area, covered by the ellipse, has a brighter ring at the edge with a finite width of around 5 µm. Here the spots still have similar irregular shapes such as those shown in Fig. 9(d). However, the corresponding SEM image of Fig. 11(c) shows that there are more and slightly larger spots present at this ring than closer to the center. From additional SEM and AFM data we conclude that these spots near the edge are more likely to correspond to a group of missing grains than to a group of grains sticking out of the surface compared to the spots found closer to the center of illumination.

The spallation spots first start to appear exactly when fluence regime II is reached for the 20 nm layer, as shown in figure 8. To investigate this further, six aluminum layers with thicknesses ranging from 10 to 30 nm were fabricated. The same pump-fluence-dependent single-shot measurements are performed to investigate the thickness-dependence of the spallation behaviour.

Optics EXPRESS

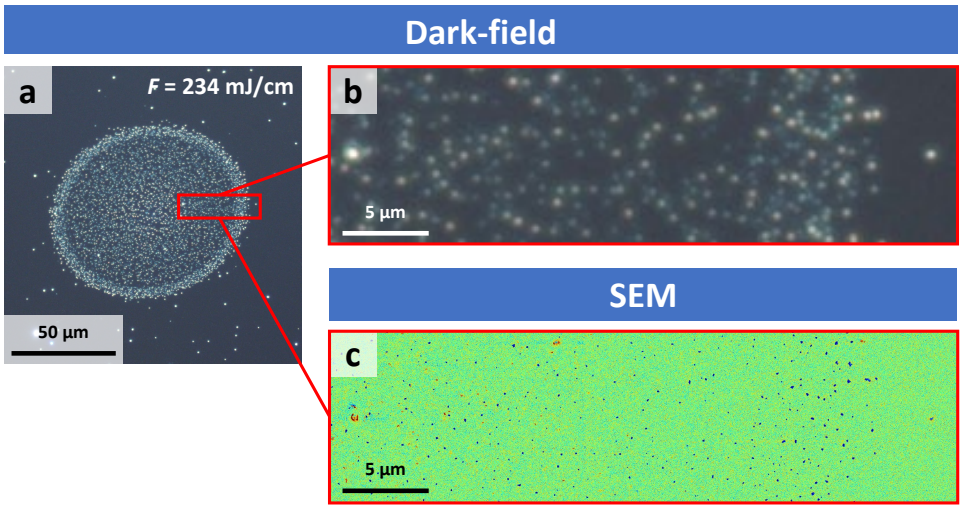

Fig. 11. (a) optical dark-field image of a regime II illuminated ($\Delta R>0$) spallated site of a 20 nm aluminum layer on borosilicate glass. The fluence used is in the high range of regime II. Near the edge of the elliptical dotted area, a bright rim appears. (b) shows a numerically zoomed-in view of the data in the red rectangle in figure (a), and (c) is the corresponding SEM image.

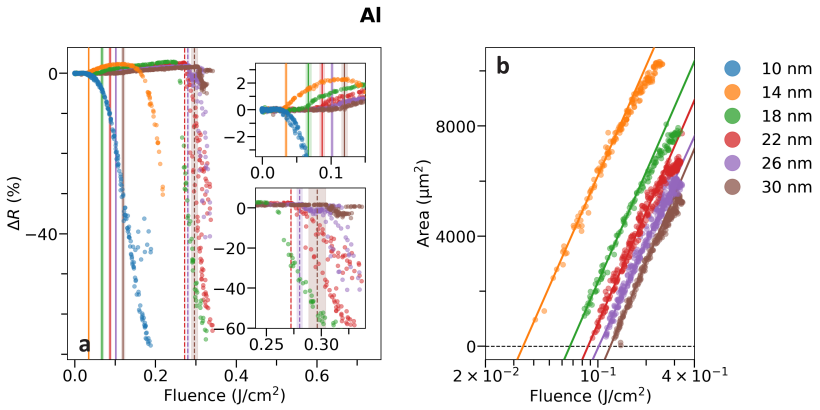

Fig. 12. (a) ΔR versus pump fluence F for 10, 14, 18, 22, 26 and 30 nm aluminum on borosilicate glass. In (a), the vertical dashed lines mark the ablation fluence F_{abl} extracted from a Liu-plot of the crater area versus fluence (not shown here). The solid lines represent the spallation fluence F_{spal} obtained from (b), which shows the Liu-plot of the spallation area as a function of fluence. The values of F_{spal} are obtained from the linear regression lines shown in (b). Note that the 10 nm Al layer is omitted in (b) because this layer displayed no clear spallation and ablation edges.

Figure 12(a) shows the measured ΔR versus the pump fluence for those layers. The spallation area A versus $\ln(F)$ is shown in the Liu-plot in Fig. 12(b), where the linear regression lines are the corresponding fits from which the spallation thresholds are determined (see section 2.4). From these linear regression lines, the spallation threshold, and from the crater areas the ablation threshold fluences F_{spal} and F_{abl}, and the FWHM of the beam profile d are obtained and given in table 3. Except for the 10 nm layer, all Al layers display a positive ΔR regime. The spallation thresholds F_{spal} extracted from the Liu-plot are shown as solid vertical lines in Fig. 12(a). In

Optics EXPRESS

this figure it is clear that the spallation thresholds strongly correlate with the offset of the $\Delta R>0$ fluence regime. This same procedure is followed to determine the ablation thresholds F_{abl} which are shown as vertical dashed lines. The $\Delta R>0$ fluence regime is bounded by F_{spal} and F_{abl}. However, in contrast to other thicknesses, the 10 nm layer does not display a positive ΔR regime. No spallation of groups of grains is observed for this layer, and for higher fluences there is no clear crater edge. SEM images of the illuminated sites show charging and optical microscopy images show an increase in transmission, all indicative of enhanced oxidation.

Table 3. Spallation and ablation threshold fluences and inferred laser illumination spot diameters for aluminum layers, obtained by Liu-analysis.

Thickness (nm)	F_{spal} (mJ/cm^2)	F_{abl} (mJ/cm^2)	d (μm)
14	34 ± 2		71.4 ± 0.3
18	67 ± 4		71.6 ± 0.4
20	72 ± 4	255 ± 5	69.9 ± 0.4
22	87 ± 3	272.3 ± 0.2	71.9 ± 0.3
26	101 ± 3	280 ± 2	70.0 ± 0.2
30	120 ± 4	296 ± 8	72.5 ± 0.3

To examine the role of the substrate on the occurrence of spallation, 20 nm-thick aluminum layers were deposited on four different substrates simultaneously: borosilicate glass, sapphire, CaF_2 and silicon, having thicknesses of 0.5, 1.1, 0.5 and 0.5 mm respectively. Sapphire is chosen because its thermal conductivity is over 40 times higher than that of borosilicate glass. Additionally, sapphire has a melting and evaporation temperature of 2300 K and 3252 K respectively, compared to the much lower value of 950 K and ≈ 2500 K for borosilicate glass [44–46]. Note that the evaporation temperatures are not reached in our experiments. CaF_2 is the only substrate with no oxygen in it, thus a possible effect of an aluminum reaction with the oxygen atoms in the substrates is excluded. Silicon is used because it is the benchmark substrate in the semiconductor industry. Here we use (100) p-doped silicon with a 1.7 nm native oxide as obtained by ellipsometry. Figure 13 shows the relative reflection change versus the pump fluence of these four samples. The difference in F_{spal} between the borosilicate glass, sapphire and CaF_2 substrates is remarkably small, indicating that the substrate plays a fairly minor role in the spallation process. Note that these three substrates are non-absorbing, transparent materials whereas silicon is not. Due to the differences in optical parameters between the substrates, the absorption of the pump-light in the 20 nm thick aluminum layer is different. Using the transfer-matrix method [20,21], the calculated total absorbed fraction of pump-light is much lower for the Al layer on silicon (9%) compared to the other substrates (15-17%). It is very likely that this difference in absorption causes the increased F_{spal} threshold of the aluminum on the silicon substrate. For all substrates used, a $\Delta R>0$ pre-ablation fluence regime is observed. All except the sapphire substrate, display groups of spallated grains in this regime (not shown here).

3.3. Calculations

As demonstrated above, when thin layers of gold or aluminum are illuminated by pump fluences below the ablation threshold, irreversible optical changes occur ($\Delta R>0$). In this fluence regime, different material and/or morphological changes such as delamination, melting, and enhanced oxidation coincide with optical changes. Morphological changes can also influence the reflectivity, and therefore ΔR directly. We performed some calculations to investigate whether these changes are directly causing this reflectivity change.

It is known that the adhesion of gold to glass is weak if no adhesion layer such as Cr or Ti is used [47]. This is confirmed by the formation of wrinkles near the ablation edges for pump fluences in

Optics EXPRESS

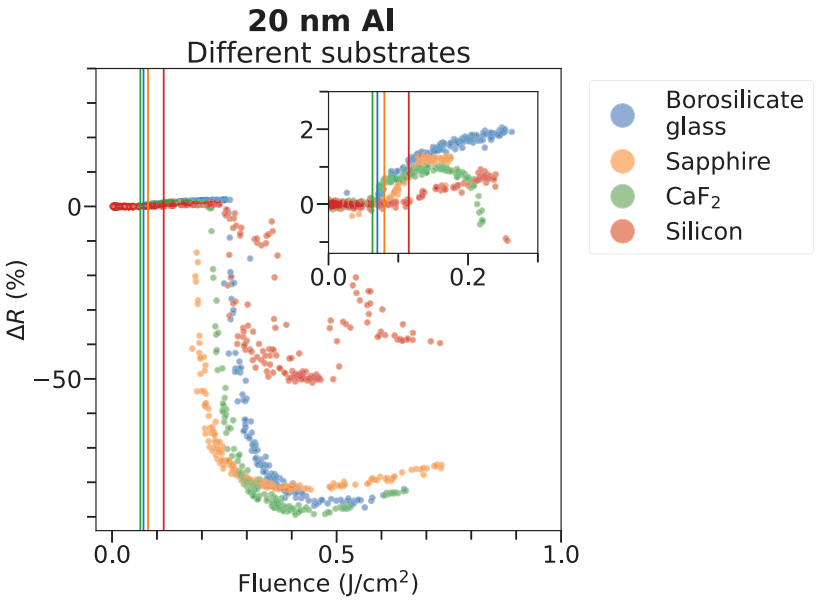

Fig. 13. Relative reflection change ΔR versus fluence F of 20 nm aluminum on 0.5 mm thick borosilicate glass, 1.1 mm thick sapphire, 0.5 mm thick CaF_2 and 0.5 mm thick silicon substrates. The start of the steep decrease marks the ablation thresholds. Below the ablation threshold, all samples display a $\Delta R>0$ fluence regime. The solid vertical lines indicate the beginning of this fluence regime F_{spal}. Ablation starts to occur from where ΔR decreases rapidly.

the ablation regime. It is therefore plausible that some delamination, which precedes ripping and wrinkling, already occurs in the pre-ablation regime. When the gold layer detaches from the substrate, a void layer is formed in between the glass substrate and the gold layer as schematically shown in Fig. 5(b). We use the transfer-matrix method [20,21] to directly calculate the reflectivity of the gold sample. Here, the used refractive index and extinction coefficient values n and k of Au are obtained from ellipsometry measurements (Ellipsometer VB-400 J.A. Woollam) and the CompleteEase analysis software [48]. To investigate whether the void will directly cause an reflection increase ($\Delta R>0$), as we measured, we compare the calculated reflectivity of gold on glass including a void, with gold on glass without a void. Figure 14 shows the ΔR versus void thickness, obtained from these calculations, for 8 to 80 nm thick gold layers on borosilicate glass. For all thicknesses, ΔR increases for an increasing void thickness. The enhanced reflection is the result of increased constructive interference in the reflected direction caused by the void. The calculations clearly indicate that small void thicknesses of $\approx$ 10 nm are already enough to explain the increased reflectivity of a few percent, as observed in the experiments. Note that the effect is smaller for thicker layers which is in reasonable agreement with our measurements. For thicker layers, significantly less light will be transmitted by the Au and therefore the interference effect is strongly reduced.

For aluminum, the above explanation seems to be unlikely as no delamination was observed for aluminum on glass. This is consistent with the fact that the adhesion of aluminum to glass is known to be strong [49,50]. In addition, we have looked into enhanced oxidation as a possible explanation for the pre-ablation ΔR increase. Transfer-matrix method calculations are performed to obtain ΔR when the upper part of the Al layer actually consists of Al_2O_3. When assuming a pristine layer with a native oxide thickness of 4 nm, these calculations show that the reflectivity would in fact decrease when there would be additional pump-induced oxidation. However, this

Optics EXPRESS

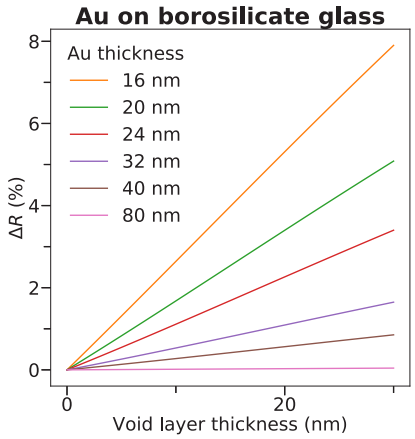

Fig. 14. Calculated relative reflection change ΔR versus the thickness of the void formed between the borosilicate glass substrate and gold. ΔR is obtained for a probe beam with a 10° angle of incidence and p-polarization. The central wavelength is 800 nm with a FWHM of 50 nm. The refractive index and extinction coefficient n and k used are obtained from ellipsometry measurements (Ellipsometer VB-400 J.A. Woollam) and the CompleteEase analysis software [48]. The 8 nm thickness calculation is omitted in this figure since this thickness is around the percolation threshold and can therefore not be considered as a fully closed layer.

is opposite to what we observe. This is not only the case for oxide growing between air and aluminum but also for oxide between the aluminum and substrate. Therefore, enhanced oxidation cannot explain the ΔR increase directly. Enhanced scattering from the spallation sites, which are clearly visible in the dark-field microscopy images, can also not be responsible for $\Delta R>0$. Both the raised grains in the 14 to 20-nm thick layers as well as the group of spallated grains in the 22 to 30 nm aluminum layers will not increase the reflectivity directly. In fact they are more likely to lower the specular reflection due to increased scattering.

Liu-analysis shows that the spallation area scales linearly with $\ln(F)$, which means that the spallation area is bordered by the threshold fluence F_{spal}. This strongly suggests that spallation is a thermally driven process. Because of this, we calculate the temperature reached in the aluminum film to further look for a possible explanation for the increased reflectivity upon laser radiation. Comparing this reached temperature with the melting temperature T_m will give insight into the spallation process. The peak temperature will already be reached in the first few picoseconds. Therefore we only calculate the temperature during the first 5 ps.

We use the two-temperature model (TTM) [23–25] to calculate the melting threshold of a 20 nm aluminum film on a borosilicate glass substrate:

$$\begin{cases} C_e(T_e)\frac{\partial T_e}{\partial t} = \frac{\partial}{\partial z}(k_e(T_e,T_i)\frac{\partial T_e}{\partial z}) - G(T_e)(T_e - T_i) + S, \\ C_i(T_i)\frac{\partial T_i}{\partial t} = G(T_e)(T_e - T_i). \end{cases} \tag{4}$$

Here $T_e = T_e(z,t)$ and $T_i = T_i(z,t)$ are the unknown temperatures of the electrons and ions respectively, as a function of depth and time. For the electronic system parametrization, we use the electron heat capacity $C_e(T_e)$ and electron-phonon coupling $G(T_e)$ from [51]. The electron thermal conductivity $k_e(T_e,T_i)$ equals $k_0\frac{T_e}{T_i}$ with $k_0 = 246$ W/mK as taken from [31]. For the ionic system we use $C_i = 2.42 \cdot 10^6$ J/m^{3}K. We neglect the ionic thermal conductivity since this is much smaller than the electronic one, k_e [31].

We use the transfer-matrix method to calculate the depth-dependent absorption profile, $A(z)$, of the laser pump energy [52]. The thickness of the film is comparable to the optical skin depth,

Optics EXPRESS

therefore the effect of light reflection and transmission at various interfaces must be considered. We calculate the absorption profile considering the full material stack, namely a thin top layer of aluminum oxide (4 nm thickness), aluminum, and a borosilicate glass substrate. We use the absorption profile in aluminum only in the heat source term $S = S(z,t)$ in the TTM Eqs. (4) as follows:

$$S(z,t) = \sqrt{\frac{4\ln(2)}{\pi}}\frac{A(z)F_0}{t_p}e^{-4\ln(2)(\frac{t}{t_p})^2}. \tag{5}$$

Here F_0 is the incident peak fluence ($F_0 = \ln(2)F$) and t_p is the pulse duration. We solve the TTM equations only for the aluminum layer, therefore, we do not take into account the heat transfer from the aluminum film into the oxide and substrate since it plays a minor role on the considered timescale of the first 5 ps. Therefore, Neumann boundary conditions: no heat flux through both aluminum interfaces, and room temperature initial conditions are applied, whereafter the set of Eqs. (4) is solved numerically. We consider only one spatial dimension, namely depth, since the laser spot size (≈ 70 μm FWHM) is much larger than the 20 nm film thickness. Therefore, we neglect lateral heat diffusion on the timescales considered.

Figure 15 shows the results of the TTM calculation for $F_0 = 34$ mJ/cm^2, where the time evolution of the electron and ion temperatures at the aluminum surface is plotted. The ion temperature increases as a result of heat transfer from the laser-heated electrons via electron-phonon coupling. The melting threshold is defined as the minimum peak fluence required to overcome the effective melting temperature $T_m^{eff} = T_m + H_m/C_i$. Here $T_m = 933.47$ K is the equilibrium melting temperature of aluminum, and $H_m = 1.07 \cdot 10^6$ kJ/m^3 is the enthalpy of melting [29, p. 6-146]. In such a way, we roughly include the enthalpy of melting effect in our melting threshold calculation. As one can see, the chosen fluence corresponds to the melting threshold defined with such a method. Because $F = F_0/\ln(2)$, this results in a calculated $F_{melting}$ of 49 mJ/cm^2 which is below our measured value of the spallation threshold $F_{spal} = 72 \pm 4$ mJ/cm^2 as shown in table 3. This means that according to these calculations, when F_{spal} is reached, the aluminum also reaches the melting temperature.

The calculation of the melting threshold is most sensitive to the choice of the electron-phonon coupling parameter G. Despite significant theoretical efforts to calculate this parameter in the regime of strong laser excitation [53], and recent experiments addressing the topic of electron-phonon coupling measurements [54], there remains a certain ambiguity in the choice of this coupling parameter practically for any material [53]. However, in the case of aluminum, several model predictions largely overlap and are consistent with the experimental results [53], therefore we believe that our choice of the coupling parameter is reliable.

We perform the same calculation to obtain the melting threshold for different aluminum thicknesses $F_{melting}$. As described before, the absorption profile is calculated with the oxide (4 nm) and substrate included, whereas the TTM calculations are performed for the aluminum layer only. The calculated $F_{melting}$ values, as well as the experimentally obtained F_{spal} are shown as a function of layer thickness in figure 16. Note that in this figure, the thickness is that of the aluminum plus its 4 nm oxide. For thicknesses between ≈ 10 and 50 nm, both the calculated melting, and measured spallation fluences follow a linear increase with thickness, where $F_{spal}/F_{melting} \approx 1.5$. The calculated melting threshold saturates at large aluminum thicknesses, corresponding to the bulk behaviour. For all measured thicknesses the spallation threshold is higher than the calculated melting threshold. This is in line with [12,55] where it is reported that melting precedes ablation.

3.4. Electron backscatter diffraction

If the reflectivity change in the $\Delta R>0$ regime, where spallation occurs, is caused by melting and resolidification of the aluminum, there might be structural change in the aluminum present. The melting temperature of aluminum oxide is 2327 K [29, p. 6-146], which is much higher

Optics EXPRESS

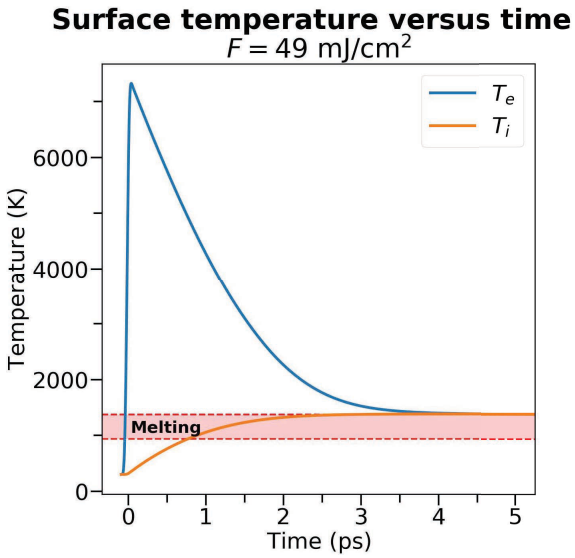

Fig. 15. Surface temperature evolution of an aluminum film calculated with the TTM at a laser fluence of F_0 = 34 mJ/cm^2 (F = 49 mJ/cm^2). The 20 nm thick layer consists of a 16 nm thick aluminum film on a borosilicate glass substrate including a 4 nm thick oxide. The lower red dashed line shows the melting temperature T_m and the upper line the effective melting temperature T_m^{eff} of aluminum used to define the melting threshold.

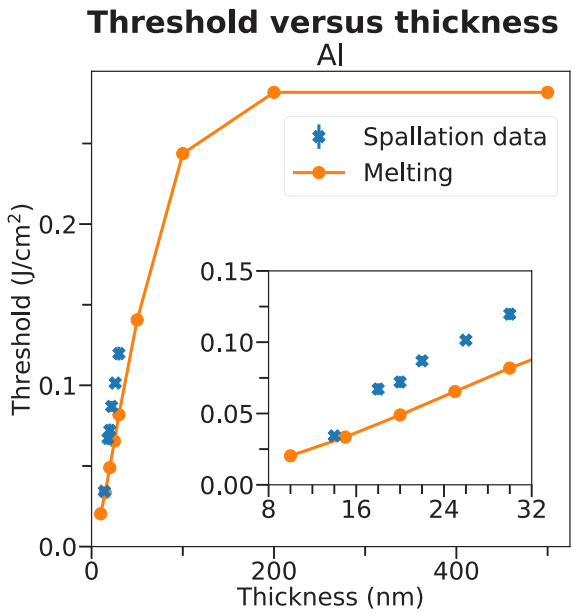

Fig. 16. Experimentally obtained spallation F_{spal} and calculated melting thresholds $F_{melting}$ versus layer thickness for aluminum on glass. The blue and orange lines are the experimentally obtained F_{spal} and the calculated $F_{melting}$ respectively. The inset zooms in on the data for small layer thicknesses, to show the differences between the calculation and measured datapoints more clearly. Note that the total thickness is that of the aluminum plus that of the native oxide layer.

Optics EXPRESS

than that of aluminum (933.47 K). This implies that the aluminum oxide structure is not significantly affected at the temperatures where Al melts, as confirmed by the AFM scans. Except for the spallated groups of grains, AFM scans did not show any surface change, like modified roughness or grain size, except for the spallated groups of grains. To determine whether the Al structure underneath the Al_2O_3 has changed, we use Electron Backscatter Diffraction (EBSD). By comparing this with the pristine material, changes in grain size and crystal orientations can be obtained. Several EBSD maps are obtained from a single ablated site on a sample of 20 nm aluminum on borosilicate glass. Figure 17(a) is a dark-field microscopy image of this site where the red rectangles indicate the positions of the corresponding EBSD maps. These scans are obtained at different distances from the center of the illuminated site. Thereby, each spot samples a different local fluence F_{local} for which $F_{local}<F_{spal}$, Fig. 17(b-c), and $F_{local}>F_{spal}$, as shown in figure d-f. From Fig. 17(d-f) it is visible that the average grain size has increased.

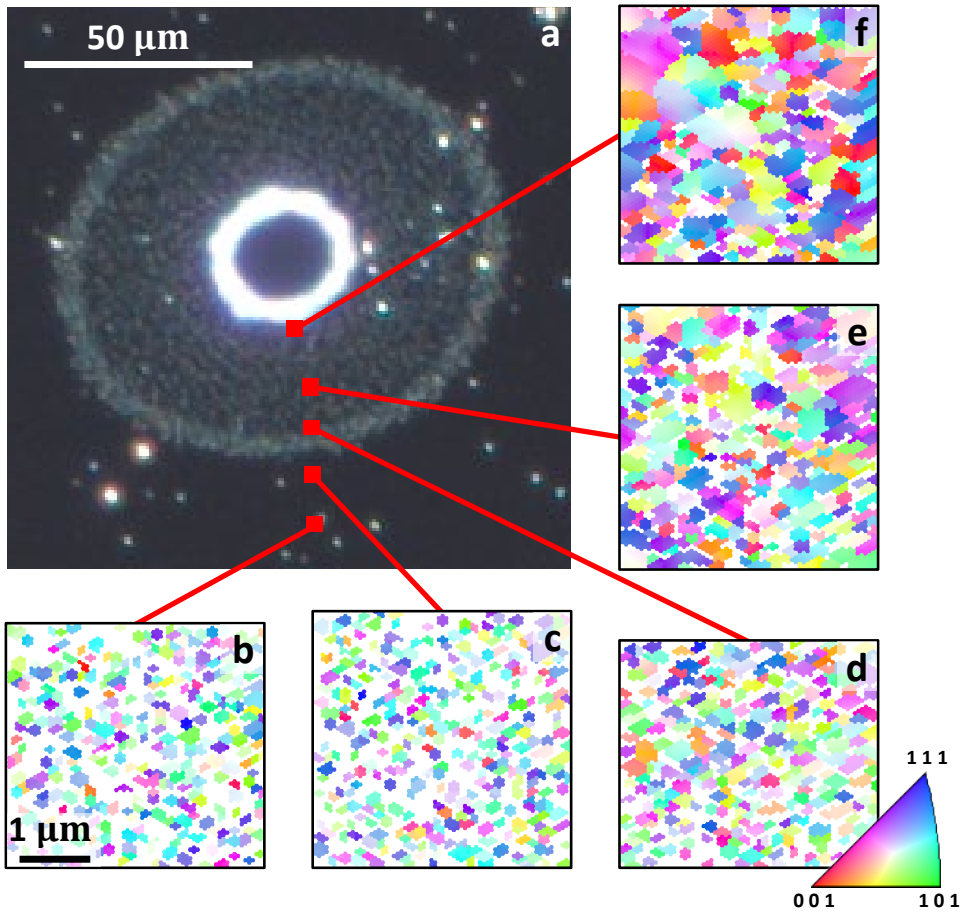

Fig. 17. The dark-field microscopy image (a) of an ablated site on a 20 nm aluminum on borosilicate glass sample. The red rectangles indicate the positions of the corresponding EBSD maps (b-f). The different colors show the different crystal orientations, while similar neighbouring pixel colors indicate that they belong to the same aluminum grain. The scans are obtained at different distances from the center of the illuminated site. Therefore, each spot samples a different local fluence F_{local} for which $F_{local}<F_{spal}$ (b-c), and $F_{local}>F_{spal}$ (d-f). From (d-f) it is clearly visible that the average grain size has increased.

Optics EXPRESS

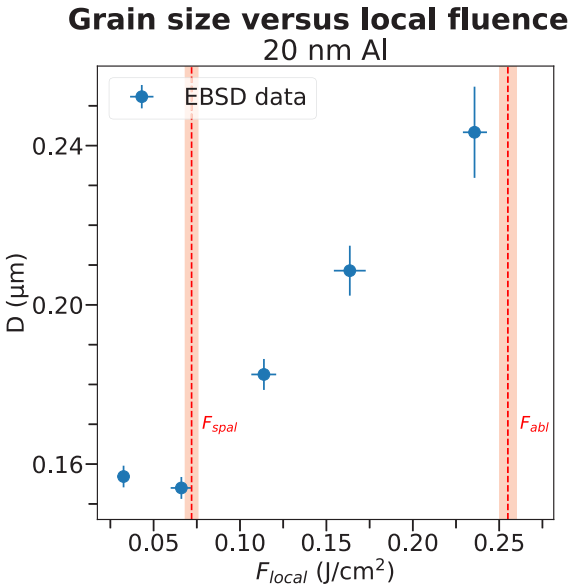

Fig. 18. The average grain size versus local fluence F_{local} obtained for each EBSD map shown in Fig. 17(b-f) of a 20 nm thick aluminum illuminated site. The values of the grain sizes are defined by the equivalent circular diameter of the grain area ($D = 2\sqrt{\frac{A_{grain}}{\pi}}$). F_{spal} and F_{abl} are the spallation and ablation fluence respectively.

All EBSD maps consists of hexagonal pixels with each having an area A_{pixel} equal to

$$A_{pixel} = \frac{\sqrt{3}}{2}s^2, \tag{6}$$

where s is the equivalent step size in the EBSD map. Multiplying this with the number of pixels N that belong to the same grain results in the total grain area A_{grain}. The grain size is expressed as the diameter D of the circle with an area equal to A_{grain}. Therefore D equals to:

$$D = 2\sqrt{\frac{N \cdot A_{pixel}}{\pi}}. \tag{7}$$

For each EBSD map shown in Fig. 17(b-f), the grain size distribution is obtained (see Supplement 1). From this, the average and spread in grain size D are obtained using the bootstrapping method. This is plotted versus the local fluence F_{local} as is shown in Fig. 18. Here it is shown that the average grain size starts to increase for local fluences exceeding F_{spal} and keeps increasing for increasing fluences. The growth of the grain size is a clear indication that single-shot annealing took place. As this fluence regime F_{local} coincides with the $\Delta R>0$ regime, it seems very likely that the increase in grain size, the microstructural change, is responsible for the slightly enhanced reflection.

To directly compare a $F_{local}>F_{abl}$ and $F_{spal}<F_{local}<F_{abl}$ site, we also performed an EBSD scan over part of the ablation edge, covering both regimes. To compare the positions of the spallated grains, two images are obtained: An EBSD map and a corresponding SEM image as is shown in Fig. 19(a and b) respectively. EBSD (a) shows increased grain sizes outside the crater, due to annealing, as well as no signal in the ablation crater. The later shows the removal of aluminum since only the aluminum creates an EBSD signal. Although, it is reported that the initially amorphous oxide layer can transform into crystalline γ-Al_2O_3 [33,34], in our case, there is an absence of EBSD patterns that correspond to γ-Al_2O_3. This confirms that Al_2O_3 still

Optics EXPRESS

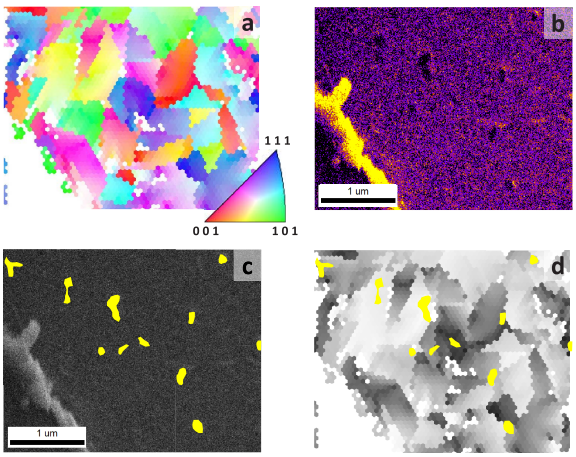

Fig. 19. EBSD map (a) and corresponding SEM image (b). (a) shows increased grain sizes outside of the crater, as well as no signal in the ablation crater indicating the removal of Al. In (b), both the ablation edge as well as the pushed-up/missing spallated sites are visible. Here, (b) is the original grayscale image converted into a colored one resulting in an enhanced image to increase the visibility of the spallated sites. (c) is the original SEM image with the spallated sites, which are drawn by hand, marked in yellow. (d) is the EBSD map in grayscale overlayed with the marked spallation grains. This shows that spallation sites are often formed at the edges or between the annealed grains.

remained amorphous and that therefore the EBSD signal only originates from the aluminum. At the SEM image (b), both the ablation edge as well as the pushed-up/missing spallated sites are visible. The original grayscale image is converted into a colored one resulting in an enhanced image to increase the visibility of the spallated sites. Figure 19(c) is the original SEM image (before enhancing) with the spallated sites, which are drawn by hand, marked in yellow. When overlaying these marks with the EBSD map (d), it shows that spallation sites often occur at the edges or between the annealed grains. Since a stress increase is necessary to remove or push-up a spallated site, this implies that local stress increase is more likely to occur at the annealed grain boundaries. Interestingly, the shape of these spallation sites mimic grain boundaries of a group of grains. As explained before, these grain boundary lines might originate from the pristine aluminum layer the oxide grew on.

4. Conclusions

We studied optical and morphological changes induced by a single ultrafast laser pulse on 8 to 80 nm thick gold and aluminum films. We have shown that the reflectivity increases with a few percent for pulses with a fluence lower than the ablation threshold. This *pre-ablation* fluence regime coincides with morphological changes. These morphological changes are observed using dark-field microscopy, SEM and AFM.

For gold, the reflectivity increase is most likely caused by delamination: the gold layer detaches from the substrate whereby a void is formed in between. The optical change is directly induced by the etalon effect caused by the creation of this void. According to transfer-matrix method calculations, the reflectivity of the weak 800 nm probe beam should increase with void thickness, which is in agreement with our measurements. Void layers as thin as $\approx$ 10 nm are already enough to cause the measured 0.1 - 2% positive relative reflection change for 8 to 80 nm thick gold layers.

For aluminum, there are no signs of delamination. However, the area, where the pre-ablation fluence threshold is exceeded, is covered with small subwavelength (50 to 200 nm) groups of

Optics EXPRESS

grains. These groups of grains are pushed up or missing entirely from the surface and their thickness matches the thickness of the native oxide (4 nm). Unlike the void with gold, these *spallation* grains do no directly explain the increase of the measured reflectivity. However, the spallation and increase in reflectivity do coincide. Liu-analysis shows that the area, covered with the spallation sites, scales linearly with $\ln(F)$. Since the pump beam has a Gaussian profile, this means that this area is bordered by the threshold fluence F_{spal}, and that the formation of these spallated sites is a thermally driven process. For a total thickness of the aluminum plus its oxide (4 nm) between 10 and 30 nm, the measured F_{spal} ranges between 34 ± 2 and 102 ± 4 mJ/cm^2. Furthermore, two-temperature model calculations show that the temperature reached in this pre-ablation fluence regime exceeds the melting temperature of aluminum. For thicknesses between $\approx$ 10 and 50 nm, both the calculated melting, and measured spallation fluences follow a linear increase with thickness, where $F_{spal}/F_{melting} \approx 1.5$. AFM and SEM cannot directly probe the structural changes caused my melting of the aluminum. This is because the aluminum is buried underneath its native oxide. Since the oxide did not reach its melting temperature, the surface of the oxide is, except for the spallation sites, unaffected. To study the changes in the aluminum underneath the oxide layer, Electron Backscatter Diffraction (EBSD) is used. EBSD shows the effects of recrystallization: the melting and resolidification of the aluminum into bigger grains. The average pristine grain size of 150 nm starts to grow where the local fluence exceeds the spallation threshold F_{spal}. The grain size grows up to 400 nm just before the ablation threshold fluence is reached.

The formation of spallation sites coincides with the increase in reflectivity, $\Delta R>0$. Still, we found no direct causality since spallation cannot increase the reflectivity directly. In fact, spallation sites are more likely to lower the specular reflection due to increased scattering while no change in surface roughness was found. The melting and resolidification of the aluminum into bigger grains, as is measured by EBSD, coincides with the $\Delta R>0$ fluence regime as well. Interestingly, it is known that different structures can lead to different optical parameters [56]. Increasing the grain size leads to a bigger mean free path of the electrons which will decrease the resistivity of our aluminum layer. Previous research has shown that a resistivity decrease increases reflectivity [57] and in [58] it follows from classical reflection theory. It is therefore possible that this microstructural change in grain size directly causes the small reflection increase observed in the measurements. The spallation sites, which consist of the native oxide, are mostly formed at the edges or in between annealed aluminum grains. Since a stress increase is necessary to remove or push-up part of the native oxide (spallation), this implies that local stress increase is more likely to occur at the annealed grain boundaries.

In summary, optical and morphological changes induced by single pump pulses already occur in the pre-ablation fluence regime. The in situ probing of the optical changes presented in this work is a quick and easy way to detect very subtle changes in thin films, making this technique suitable to use as an early warning signal for catastrophic damage. Monitoring this signal can be of use in the semiconductor manufacturing industry, since these thin films are exposed to increasingly high optical powers used in metrology, which heightens the risk of optical damage.

Funding. Nederlandse Organisatie voor Wetenschappelijk Onderzoek (019.211EN.026, 17963, 19459).

Acknowledgements. This publication is part of the project "Wafer damage control: understanding and preventing light-induced material changes in optical measurement systems" (with project number 17963) of the research program High Tech Systems and Materials (HTSM) which is (partly) financed by the Dutch Research Council (NWO). The project is co-financed by ASML and ASM Laser Separation International (ALSI). Electron Backscatter Diffraction characterization is part of the project "Achieving Semiconductor Stability From The Ground Up" (with project number 19459) which is financed by the Dutch Research Council (NWO), Gatan (EDAX), Amsterdam Scientific Instruments (ASI) and CL Solutions. IM gratefully acknowledges the financial support from the Dutch Research Council (NWO) (Project 'PROMT', Grant Rubicon Science 2021-1 S, file number 019.211EN.026). The authors thank Marnix Vreugdenhil, Dries van Oosten and Vina Faramarzi for the interesting discussions and for careful reading of the manuscript and Thomas Meijvogel, Igor Hoogsteder and Dylan Loozen for technical support.

Optics EXPRESS

Disclosures. The authors have no conflicts to disclose.

Data Availability. Data underlying the results presented in this paper may be obtained from the authors upon reasonable request.

Supplemental document. See Supplement 1 for supporting content.

References

1. H. Dachraoui and W. Husinsky, "Fast electronic and thermal processes in femtosecond laser ablation of au," Appl. Phys. Lett. **89**(10), 104102 (2006).
2. J. Güdde, J. Hohlfeld, J. Müller, *et al.*, "Damage threshold dependence on electron–phonon coupling in au and ni films," Appl. Surf. Sci. **127-129**, 40–45 (1998).
3. A. A. Ionin, S. I. Kudryashov, S. V. Makarov, *et al.*, "Nanoscale surface boiling in sub-threshold damage and above-threshold spallation of bulk aluminum and gold by single femtosecond laser pulses," Laser Phys. Lett. **13**(2), 025603 (2016).
4. V. Whitley, S. McGrane, D. Eakins, *et al.*, "The elastic-plastic response of aluminum films to ultrafast laser-generated shocks," J. Appl. Phys. **109**(1), 013505 (2011).
5. J. Winter, S. Rapp, M. Spellauge, *et al.*, "Ultrafast pump-probe ellipsometry and microscopy reveal the surface dynamics of femtosecond laser ablation of aluminium and stainless steel," Appl. Surf. Sci. **511**, 145514 (2020).
6. X. Zhao and Y. C. Shin, "Femtosecond laser ablation of aluminum in vacuum and air at high laser intensity," Appl. Surf. Sci. **283**, 94–99 (2013).
7. D. Von der Linde and K. Sokolowski-Tinten, "The physical mechanisms of short-pulse laser ablation," Appl. Surf. Sci. **154-155**, 1–10 (2000).
8. B. N. Chichkov, C. Momma, S. Nolte, *et al.*, "Femtosecond, picosecond and nanosecond laser ablation of solids," Appl. Phys. A **63**(2), 109–115 (1996).
9. S. Sonntag, J. Roth, F. Gaehler, *et al.*, "Femtosecond laser ablation of aluminium," Appl. Surf. Sci. **255**(24), 9742–9744 (2009).
10. S. Kudryashov and A. Ionin, "Multi-scale fluence-dependent dynamics of front-side femtosecond laser heating, melting and ablation of thin supported aluminum film," Int. J. Heat Mass Transf. **99**, 383–390 (2016).
11. M. Stafe, I. Vladoiu, and I. M. Popescu, "Impact of the laser wavelength and fluence on the ablation rate of aluminium," Cent. Eur. J. Phys. **6**(2), 327–331 (2008).
12. I. Milov, V. Zhakhovsky, D. Ilnitsky, *et al.*, "Two-level ablation and damage morphology of ru films under femtosecond extreme uv irradiation," Appl. Surf. Sci. **528**, 146952 (2020).
13. F. Akhmetov, I. Milov, S. Semin, *et al.*, "Laser-induced electron dynamics and surface modification in ruthenium thin films," Vacuum **212**, 112045 (2023).
14. Y. Gan and J. K. Chen, "Nonequilibrium phase change in gold films induced by ultrafast laser heating," Opt. Lett. **37**(13), 2691–2693 (2012).
15. A. Kuznetsov, J. Koch, and B. Chichkov, "Nanostructuring of thin gold films by femtosecond lasers," Appl. Phys. A **94**(2), 221–230 (2009).
16. T. Pflug, J. Wang, M. Olbrich, *et al.*, "Case study on the dynamics of ultrafast laser heating and ablation of gold thin films by ultrafast pump-probe reflectometry and ellipsometry," Appl. Phys. A **124**(2), 116 (2018).
17. M. Olbrich, T. Pflug, C. Wüstefeld, *et al.*, "Hydrodynamic modeling and time-resolved imaging reflectometry of the ultrafast laser-induced ablation of a thin gold film," Opt. Lasers Eng. **129**, 106067 (2020).
18. E. Silaeva, L. Saddier, and J.-P. Colombier, "Drude-lorentz model for optical properties of photoexcited transition metals under electron-phonon nonequilibrium," Appl. Sci. **11**(21), 9902 (2021).
19. J. Chen, W.-K. Chen, J. Tang, *et al.*, "Time-resolved structural dynamics of thin metal films heated with femtosecond optical pulses," Proc. Natl. Acad. Sci. U.S.A. **108**(47), 18887–18892 (2011).
20. S. J. Byrnes, "Multilayer optical calculations," arXiv, arXiv:1603.02720 (2016).
21. M. Born and E. Wolf, *Principles of Optics* (Cambridge University Press, Cambridge, UK, 1980), sixth ed.
22. J. M. Liu, "Simple technique for measurements of pulsed gaussian-beam spot sizes," Opt. Lett. **7**(5), 196–198 (1982).
23. M. Kaganov, "Relaxation between electrons and the crystalline lattice," Sov. Phys. JETP **4**, 173–178 (1957).
24. S. I. Anisimov, "Effect of the powerful light fluxes on metals," Sov. Phys. Tech. Phys. **11**, 945 (1967).
25. S. Anisimov, B. Kapeliovich, T. Perelman, *et al.*, "Electron emission from metal surfaces exposed to ultrashort laser pulses," Zh. Eksp. Teor. Fiz **66**, 375–377 (1974).
26. E. Inc., *Microscope Slides and Coverslips* (2021).
27. P. B. Johnson and R.-W. Christy, "Optical constants of the noble metals," Phys. Rev. B **6**(12), 4370–4379 (1972).
28. F. Cheng, P.-H. Su, J. Choi, *et al.*, "Epitaxial growth of atomically smooth aluminum on silicon and its intrinsic optical properties," ACS Nano **10**(11), 9852–9860 (2016).
29. W. M. Haynes, *CRC handbook of chemistry and physics* (CRC press, 2014), 95th ed.
30. J. Hohlfeld, S.-S. Wellershoff, J. Güdde, *et al.*, "Electron and lattice dynamics following optical excitation of metals," Chem. Phys. **251**(1-3), 237–258 (2000).
31. A. Jain and A. J. McGaughey, "Thermal transport by phonons and electrons in aluminum, silver, and gold from first principles," Phys. Rev. B **93**(8), 081206 (2016).

Optics EXPRESS

32. H. E. Elsayed-Ali, T. Juhasz, G. O. Smith, *et al.*, "Femtosecond thermoreflectivity and thermotransmissivity of polycrystalline and single-crystalline gold films," Phys. Rev. B **43**(5), 4488–4491 (1991).
33. L. Nguyen, T. Hashimoto, D. N. Zakharov, *et al.*, "Atomic-scale insights into the oxidation of aluminum," ACS Appl. Mater. Interfaces **10**(3), 2230–2235 (2018). PMID: 29319290.
34. L. Jeurgens, W. Sloof, F. Tichelaar, *et al.*, "Structure and morphology of aluminium-oxide films formed by thermal oxidation of aluminium," Thin Solid Films **418**(2), 89–101 (2002).
35. J. Canny, "A computational approach to edge detection," IEEE Trans. Pattern Anal. Mach. Intell. **PAMI-8**(6), 679–698 (1986).
36. R. Halır and J. Flusser, "Numerically stable direct least squares fitting of ellipses," in *Proc. 6th International Conference in Central Europe on Computer Graphics and Visualization. WSCG*, vol. 98 (Citeseer, 1998), pp. 125–132.
37. P. Gadenne, Y. Yagil, and G. Deutscher, "Transmittance and reflectance insitu measurements of semicontinuous gold films during deposition," J. Appl. Phys. **66**(7), 3019–3025 (1989).
38. K. H. Bennemann, *Non-linear optics in metals*, 98 (Oxford University Press, 1998).
39. E. D. Palik, *Handbook of optical constants of solids*, vol. 3 (Academic press, 1998).
40. S. Zhang, Y. Pei, and L. Liu, "Dielectric function of polycrystalline gold films: Effects of grain boundary and temperature," J. Appl. Phys. **124**(16), 165301 (2018).
41. G. De Haan, J. Hernandez-Rueda, and P. Planken, "Femtosecond time-resolved pump-probe measurements on percolating gold in the ablation regime," Opt. Express **28**(8), 12093–12107 (2020).
42. M. Voncken and V. Faramarzi, Private Communication (2021).
43. W. Xu, P. M. Wood-Adams, and C. G. Robertson, "Measuring local viscoelastic properties of complex materials with tapping mode atomic force microscopy," Polymer **47**(13), 4798–4810 (2006).
44. Ossila, "Sapphire substrates," https://www.ossila.com/en-eu/products/sapphire-substrates. Visited 22-12-2022.
45. P. S. Technologies, "About sapphire," https://www.sapphire.lt/sapphire/. Visited 07-12-2023.
46. C. BooK, "Silica glass(60676-86-0)," https://www.chemicalbook.com/ProductMSDSDetailCB1199394_EN.htm. Visited 07-12-2023.
47. Q. Jiang, B. Rogez, J.-B. Claude, *et al.*, "Adhesion layer influence on controlling the local temperature in plasmonic gold nanoholes," Nanoscale **12**(4), 2524–2531 (2020).
48. E. Complete, "Software manual version 3.18, ja woollam co," (2007).
49. I. Hoogsteder, Private Communication (2022).
50. D. M. Mattox, "Chapter 12 - adhesion and deadhesion," in *Handbook of Physical Vapor Deposition (PVD) Processing (Second Edition)*, D. M. Mattox, ed. (William Andrew Publishing, Boston, 2010), p. 464, second edition ed.
51. Z. Lin, L. V. Zhigilei, and V. Celli, "Electron-phonon coupling and electron heat capacity of metals under conditions of strong electron-phonon nonequilibrium," Phys. Rev. B **77**(7), 075133 (2008).
52. L. Alber, "Absorptiontmm," https://github.com/udcm-su/AbsorptionTMM (2019).
53. N. Medvedev and I. Milov, "Electron-phonon coupling in metals at high electronic temperatures," Phys. Rev. B **102**(6), 064302 (2020).
54. M. Z. Mo, Z. Chen, R. K. Li, *et al.*, "Heterogeneous to homogeneous melting transition visualized with ultrafast electron diffraction," Science **360**(6396), 1451–1455 (2018).
55. M. Agranat, S. Anisimov, S. Ashitkov, *et al.*, "Dynamics of plume and crater formation after action of femtosecond laser pulse," Appl. Surf. Sci. **253**(15), 6276–6282 (2007).
56. A. Lehmuskero, M. Kuittinen, and P. Vahimaa, "Refractive index and extinction coefficient dependence of thin al and ir films on deposition technique and thickness," Opt. Express **15**(17), 10744–10752 (2007).
57. P. Schmitt, S. Stempfhuber, N. Felde, *et al.*, "Influence of seed layers on the reflectance of sputtered aluminum thin films," Opt. Express **29**(13), 19472–19485 (2021).
58. T. T. Hu, J. H. Hsu, J. C. Huang, *et al.*, "Correlation between reflectivity and resistivity in multi-component metallic systems," Appl. Phys. Lett. **101**(1), 011902 (2012).